

# Multiparticle azimuthal correlations in isobaric $^{96}\text{Ru}+^{96}\text{Ru}$ and $^{96}\text{Zr}+^{96}\text{Zr}$ collisions at $\sqrt{s_{NN}} = 200$ GeV

Zaining Wang<sup>1</sup>, Jinhui Chen<sup>1,2</sup>, Jianguyong Jia<sup>3,4</sup>, Yu-Gang Ma<sup>1,2</sup>, Chunjian Zhang<sup>a,1,2</sup>

<sup>1</sup>Key Laboratory of Nuclear Physics and Ion-beam Application (MOE), and Institute of Modern Physics, Fudan University, Shanghai 200433, China

<sup>2</sup>Shanghai Research Center for Theoretical Nuclear Physics, NSFC and Fudan University, Shanghai 200438, China

<sup>3</sup>Department of Chemistry, Stony Brook University, Stony Brook, NY 11794, USA

<sup>4</sup>Physics Department, Brookhaven National Laboratory, Upton, NY 11976, USA

23 September 2024

**Abstract** Correlations between event-by-event fluctuations in the amplitudes of flow harmonics offer a novel way to access initial state properties in heavy-ion collisions. We have extensively predicted correlations in different flow harmonics based on multiparticle cumulants in  $^{96}\text{Ru}+^{96}\text{Ru}$  and  $^{96}\text{Zr}+^{96}\text{Zr}$  collisions at  $\sqrt{s_{NN}} = 200$  GeV from a multiphase transport model. The state-of-the-art correlated nuclear distributions for the isobars were used to show the difference in nuclear deformations and neutron skin thickness, which have distinct characteristics seen in multiparticle azimuthal correlation. We also found a minimal effect of the shear viscosity effect on these multiparticle azimuthal correlations. Therefore, these studies could also serve as an additional tool for understanding the nature of the initial state fluctuations and nuclear structure, as well as input for possible in-depth dynamical studies for experimental measurement.

**Keywords** Multiparticle azimuthal correlations · heavy ion collisions · nuclear structure

## 1 Introduction

Anisotropic flow provides key insights into the properties of the hot and dense matter, the quark-gluon plasma (QGP), in the ultra-relativistic heavy-ion collision. The initial pressure gradients in nearly ideal hydrodynamics transform the initial shape into azimuthal modulations in the distributions of the final generated particles, typically described by the Fourier series decomposition  $dN/d\phi \propto 1 + 2 \sum_{n=1}^{\infty} v_n \cos n(\phi - \Psi_n)$ , where  $N$  is the number of particles produced,  $\phi$  is the azimuthal angle of the particle,  $v_n$  and  $\Psi_n$  represent the

magnitude and the event-plane angle of the  $n^{\text{th}}$  flow harmonic [1, 2, 3], respectively. The anisotropic flow shows a good approximate proportionality to the initial state eccentricities  $\epsilon_n$ , i.e.,  $v_n \simeq \kappa_n \epsilon_n$  ( $n=2,3$ ), where the response coefficient  $\kappa_n$  depends on the transport properties, such as a shear viscosity to entropy density ratio  $\eta/s$  [4], and the equation of state [5, 6]. Experimental measurements in the “flow paradigm” of produced particles from the Relativistic Heavy Ion Collider (RHIC) [7, 8, 9, 10] and the Large Hadron Collider (LHC) [11, 12, 13] are extremely rich in numerous novel observables, such as single flow harmonics, event-by-event flow fluctuations, and flow harmonic correlations, to shed light on the characterization of the initial conditions and QGP transport properties throughout decades.

The distributions of the nucleons, which are controlled by the structure of the colliding atomic nuclei, are the natural sources of the anisotropies and the transverse size of the overlap zone in the initial state. In the quantum many-body system, the nuclear structure is a fundamental property of the atomic nuclei, reflecting the collective and correlated nature of the dynamics of nucleons. The prominent characteristic of the nuclear structure has been recently measured to explore an unanticipated link between the low-energy ground-state nuclear structure and the high-energy nuclear collisions at different energy scales. The novel fingerprints of nuclear structure in heavy-ion collisions, in fact, have been discussed by exploring bulk and hard observables [14, 15, 16, 17, 18, 19, 20, 21, 22, 23, 24, 25, 26, 27, 28, 29, 30, 31, 32, 33, 34, 35, 36, 37, 38, 39, 40, 41] within the prior state-of-the-art hydrodynamic models.

Experimental measurements with detailed comparisons between  $^{238}\text{U}+^{238}\text{U}$  and  $^{197}\text{Au}+^{197}\text{Au}$  collisions at RHIC [42, 43], and between  $^{129}\text{Xe}+^{129}\text{Xe}$  and  $^{208}\text{Pb}+^{208}\text{Pb}$  collisions at LHC [44, 45, 46] have shown signatures com-

<sup>a</sup>e-mail: chunjianzhang@fudan.edu.cn

patible with nuclear quadrupole and triaxial deformations. The isobaric collisions performed at RHIC with the same mass number,  $^{96}\text{Ru}+^{96}\text{Ru}$  and  $^{96}\text{Zr}+^{96}\text{Zr}$  collisions, have also directly reflected the visible nuclear structure difference, including quadrupole and octupole deformations, and neutron skin thickness, from the difference in the measured ratios of the final state bulk observables at a given centrality, since the systematics from hadron evolution is expected to be completely canceled out [47, 48, 49, 50]. However, the extensive understanding of anisotropic flow-related observables in isobaric collisions has not yet been explored.

In this work, we use detailed isobars  $^{96}\text{Ru}+^{96}\text{Ru}$  and  $^{96}\text{Zr}+^{96}\text{Zr}$  simulations at  $\sqrt{s_{NN}} = 200$  GeV with a multi-phase transport (AMPT) framework to study the correlated long-range mixed-harmonic fluctuations as supplementary observables, such as asymmetric cumulants, symmetric cumulants, and nonlinear coupling coefficients, that are sensitive to the initial state and could be used to further constrain nuclear structure parameters. The efficacy of the shear viscosity effect on the isobar ratios is also discussed. This paper is organized as follows. We first introduce the general AMPT model setup and the details of the analysis method employed. The results and discussions are presented, followed by a summary.

## 2 Methods

The AMPT transport model [51] is a hybrid model with four main phases: (i) fluctuating initial conditions from the HIJING model [52], (ii) elastic parton cascade simulated by the ZPC model [53], (iii) quark coalescence model for hadronization [54, 55], and (iv) hadronic rescattering based on the ART model [56]. The spatial distribution of nucleons is sampled using a deformed Woods-Saxon (WS) density profile of the form

$$\rho(r, \theta) = \frac{\rho_0}{1 + e^{[r - R_0(1 + \beta_2 Y_{2,0}(\theta) + \beta_3 Y_{3,0}(\theta))/a_0]}}, \quad (1)$$

where  $\rho_0$  denotes the nucleon density at the center of the nucleus, and  $a_0$  is the surface diffuseness parameter, also known as the skin depth. The half-density nucleus radius is  $R_0 = 1.2A^{1/3}$  where  $A$  is the mass number. The  $\beta_n$  values can be estimated from the measured reduced electric transition probability  $B(E_n) \uparrow$  via the standard formula  $\beta_n = (4\pi/3ZeR_0^n) \sqrt{B(E_n) \uparrow}$  with  $Z$  the charge number of the nucleus [57].  $\beta_2$  and  $\beta_3$  represent the quadrupole and octupole deformation parameters respectively and account for the deformation in the nuclear geometry. The deviation from the spherical axially symmetric components is parameterized by spherical harmonics expressed as  $Y_{2,0}(\theta) = \frac{1}{4}\sqrt{\frac{5}{\pi}}(3\cos^2\theta - 1)$

and  $Y_{3,0}(\theta) = \frac{1}{4}\sqrt{\frac{7}{\pi}}(5\cos^3\theta - 3\cos\theta)$ , where  $\theta$  is the polar angle with the symmetry axis.

**Table 1** Nuclear structure parameters in Eq. (1) used in the simulations of  $^{96}\text{Ru}+^{96}\text{Ru}$  and  $^{96}\text{Zr}+^{96}\text{Zr}$  collisions at  $\sqrt{s_{NN}} = 200$  GeV. Case1 and Case5 represent, respectively, the full parameterizations of  $^{96}\text{Ru}$  and  $^{96}\text{Zr}$ .

	$R_0$ (fm)	$a_0$ (fm)	$\beta_2$	$\beta_3$
Case1 $^{96}\text{Ru}$	5.09	0.46	0.162	0
Case2	5.09	0.46	0.06	0
Case3	5.09	0.46	0.06	0.20
Case4	5.09	0.52	0.06	0.20
Case5 $^{96}\text{Zr}$	5.02	0.52	0.06	0.20

Ratios	$\frac{\text{Case1}}{\text{Case2}}$	$\frac{\text{Case1}}{\text{Case3}}$	$\frac{\text{Case1}}{\text{Case4}}$	$\frac{\text{Case1}}{\text{Case5}}$
--------	-------------------------------------	-------------------------------------	-------------------------------------	-------------------------------------

Following our previous work [31, 47, 58, 59], we simulate the isobaric collisions using the AMPT version v2.26t5 using string-melting mode with 200M minimum bias events for each case. The partonic cross-section of  $3$  mb evaluated using  $\sigma = 9/2\pi\alpha_s^2/\mu^2$ , where  $\alpha_s$  is the QCD coupling constant and  $\mu$  is the screening mass, has been used here. This model could successfully reproduce the  $v_2$  data at RHIC and LHC energies [60, 61, 62, 63, 64]. The detailed five choices of the  $\beta_2$ ,  $\beta_3$ ,  $R_0$ , and  $a_0$  nuclear parameters are listed in Table 1. It allows us to isolate the influences of the nuclear structure parameters step-by-step, e.g., Case1/Case2 indicates the  $\beta_2$  effect, Case1/Case3 indicates the effects of  $\beta_2$  and  $\beta_3$ , Case1/Case4 indicates the effects of the  $\beta_2$ ,  $\beta_3$  and  $a_0$ , and Case1/Case5 indicates the effects of the  $\beta_2$ ,  $\beta_3$ ,  $a_0$  and  $R_0$ .

In addition, we also study the  $\eta/s$  dependence of flow harmonics. For a system of two massless quark flavors at initial temperature  $T$ , the  $\eta/s$  can be estimated using the following pocket formula [65]

$$\frac{\eta}{s} \approx \frac{3\pi}{40\alpha_s^2} \frac{1}{\left(9 + \frac{\mu^2}{T^2}\right) \ln\left(\frac{18 + \mu^2/T^2}{\mu^2/T^2}\right) - 18}. \quad (2)$$

Assuming an initial temperature of  $T = 0.38$  GeV, this would correspond to a  $\eta/s$  value of 0.232 at an early time. Correspondingly, the case of  $1.5$  mb gives a larger  $\eta/s$  value, while the cases of  $6.0$  mb and  $10.0$  mb give smaller  $\eta/s$  values [65] as shown in Table 2. Note that the exact values of the shear viscosities are irrelevant, what is important is that these choices significantly allow checking the stability of the isobar ratios.

The two- and multiparticle correlations are used in the current work. The framework for the cumulants is described in Ref. [66]. The formalism of the multiparti-

**Table 2** The parameter settings in the AMPT model, where the  $\eta/s$  value is estimated from Eq. (2) assuming an initial temperature of  $T = 0.38$  GeV.

$\alpha_s$	$\mu$ (fm $^{-1}$ )	$\sigma$ (mb)	$\eta/s$ (Eq. (2))
0.33	3.226	1.5	0.387
0.33	2.265	3.0	0.232
0.33	1.602	6.0	0.156
0.48	1.800	10	0.087

cle azimuthal correlations is evaluated as follows:

$$\begin{aligned} \langle v_n^2 \rangle &= \langle \langle \{2\}_n \rangle \rangle = \langle \langle e^{in(\phi_i - \phi_j)} \rangle \rangle, \\ asc_{nm,n+m} &= \langle \langle \{3\}_{n,m} \rangle \rangle = \langle \langle e^{in\phi_i + im\phi_j - i(n+m)\phi_k} \rangle \rangle, \\ \langle v_n^2 v_m^2 \rangle &= \langle \langle \{4\}_{n,m} \rangle \rangle = \langle \langle e^{in(\phi_i - \phi_j) + im(\phi_k - \phi_m)} \rangle \rangle. \end{aligned} \quad (3)$$

The double angular brackets  $\langle \langle \rangle \rangle$  indicate that the averaging procedure has been performed over an ensemble of events with similar centrality. The non-linear coupling coefficients and four-particle symmetric cumulants are defined as:

$$\chi_{n+m} = \frac{asc_{nm,n+m}}{\langle v_n^2 v_m^2 \rangle}, \quad (4)$$

$$sc_{n,m}\{4\} = \langle v_n^2 v_m^2 \rangle - \langle v_n^2 \rangle \langle v_m^2 \rangle.$$

To scale out the dependence on the single particle flow harmonics, the normalized symmetric cumulant is defined as follows:

$$nsc_{n,m}\{4\} = \frac{sc_{n,m}\{4\}}{\langle v_n^2 \rangle \langle v_m^2 \rangle}. \quad (5)$$

In order to reduce short-range “non-flow” correlations, pseudorapidity gaps are often explicitly required between the particles in each pair in the well-developed subevent cumulant methods [67]. In the two-subevent cumulant method, the tracks are divided into two subevents  $\eta_a$  and  $\eta_b$  according to  $-2 < \eta_a < 0$  and  $0 \leq \eta_b < 2$ . Only hardons with  $0.2 < p_T < 2$  GeV/c are chosen. The simulated events are binned in classes defined by the number of participated nucleons  $N_{\text{part}}$ .

### 3 Results

We focus on multiparticle cumulant calculations, which are not strongly sensitive to the hydrodynamic response. These observables are calculated in different nuclear parameters as shown in Tab. 1.  $^{96}\text{Ru}$  and  $^{96}\text{Zr}$  in full parameterizations of nuclear parameters are labeled as case1 and case5 where their statistics are shown in black and red bands. Figure 1 predicts the values of the asymmetric cumulant  $asc_{nm,n+m}\{3\}$  for  $n, m = 2, 2$  and  $2, 3$

representing the influence of nuclear structures as a function of  $N_{\text{part}}$  in  $0.2 < p_T < 2$  GeV/c. The  $asc_{nm,n+m}\{3\}$  value is positive over the entire centrality range. The correlation is weak in the central collisions, increases rapidly in the mid-central collisions, and then decreases towards more peripheral collisions. The  $asc_{nm,n+m}\{3\}$  is related to the nonlinear mode-mixing effects  $V_4 = V_{4L} + \chi_4 (V_2)^2$  and  $V_5 = V_{5L} + \chi_5 V_2 V_3$  [26, 25, 68, 69, 70]. The nonlinear coupling coefficients  $\chi_4$  and  $\chi_5$  determine the coupling strength between generated elliptic and quadrangular flow during the QGP expansion as shown in the Fig. 2. Thus, they do indeed probe the transport and hadronization properties of the QGP. They show a weak centrality dependence, with only a decrease in the 0-5% centrality range, consistent with the recent measurements [8, 71] in Au+Au and Pb+Pb collisions. The detailed effects of nuclear structure parameters via isobar ratios,  $R_{\mathcal{O}}(N_{\text{part}}) = \mathcal{O}_{\text{Ru}}(N_{\text{part}}) / \mathcal{O}_{\text{Zr}}(N_{\text{part}})$ , can be accessed extensively [26].

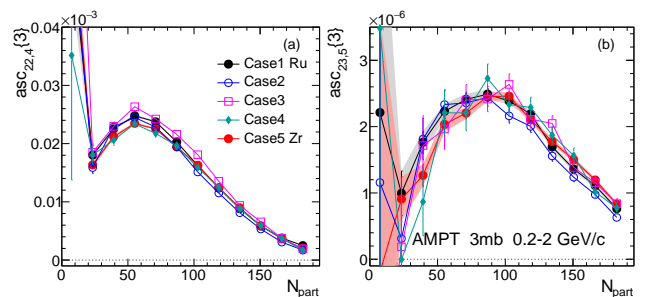


**Fig. 1** Asymmetric cumulant  $asc_{nm,n+m}\{3\}$  representing the influence of nuclear structures as a function of  $N_{\text{part}}$  in  $0.2 < p_T < 2$  GeV/c in isobaric collisions. The effects of various Woods-Saxon parameters in Table. 1 are shown.

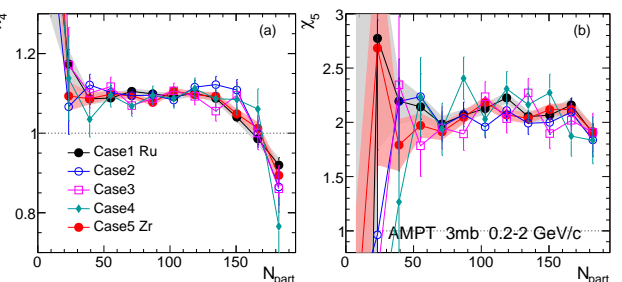


**Fig. 2** Nonlinear coupling coefficients  $\chi_4$  (left panel) and  $\chi_5$  representing the influence of nuclear structures as a function of  $N_{\text{part}}$  in  $0.2 < p_T < 2$  GeV/c in isobaric collisions. The effects of various Woods-Saxon parameters in Table. 1 are shown.

Figure 3 shows the symmetric cumulant  $sc_{n,m}\{4\}$  for  $n, m = 2, 3$  and  $2, 4$  (top panels) and their isobar ra-

tios (bottom panels) as a function of  $N_{part}$ . A negative correlation between  $v_2$  and  $v_3$ ,  $sc_{2,3}\{4\}$ , and a positive correlation between  $v_2$  and  $v_4$ ,  $sc_{2,4}\{4\}$  are observed for all collisions modes studied and over full  $N_{part}$  range. Any hydrodynamic response is expected to be canceled out by the ratios between two isobars. As can be seen in Fig. 3 (c,d), the ratios directly represent the influence of the nuclear structures in  $^{96}\text{Ru}$  and  $^{96}\text{Zr}$  nuclei. For a difference in octupole deformation  $\beta_3$ , the value of  $sc_{2,3}\{4\}$  is suppressed by 50% in the central collisions, while the value of neutron skin thickness and nuclear radius are canceled out. The values of the  $sc_{2,4}\{4\}$  ratios also reveal the complex dependence on the nuclear structure parameters. The quadrupole deformation  $\beta_2$  enhances the  $sc_{2,4}\{4\}$  in central collisions, while the octupole deformation  $\beta_3$  affects it in an opposite direction. The skin thickness increases the  $sc_{2,4}\{4\}$  in the peripheral collision, and the nuclear radius compensates the effect.

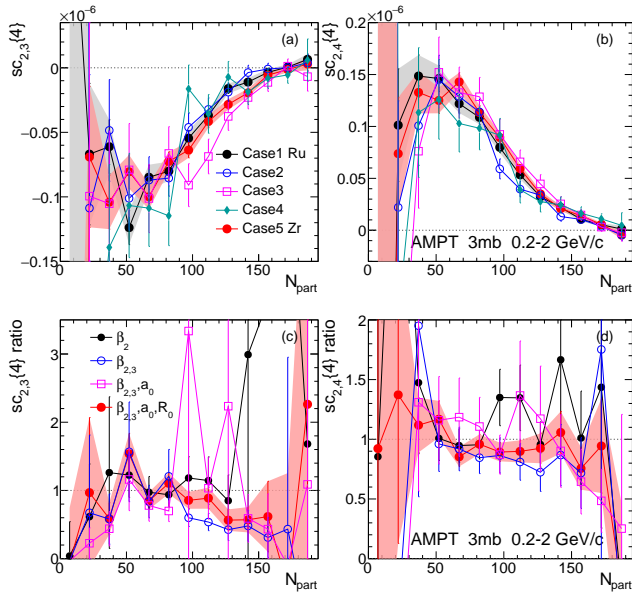


**Fig. 3** Symmetric cumulant  $sc_{n,m}\{4\}$  (a, b) and the ratios between  $^{96}\text{Ru}+^{96}\text{Ru}$  and  $^{96}\text{Zr}+^{96}\text{Zr}$  (c, d) representing the influence of nuclear structures as a function of  $N_{part}$  in  $0.2 < p_T < 2$  GeV/c. The effects of various Woods-Saxon parameters in Table. 1 are shown.

To further investigate the strength of the correlation and to separate the contribution from the magnitudes of the flow harmonics, The normalized cumulants  $nsc_{2,3}\{4\}$  and  $nsc_{2,4}\{4\}$  are studied and shown in Fig. 4. The  $nsc_{2,3}\{4\}$  and  $nsc_{2,4}\{4\}$  show a centrality dependence similar to the unnormalized case. The  $nsc_{2,3}\{4\}$  value is negative and the  $nsc_{2,4}\{4\}$  value is positive in overall centrality range. The  $nsc_{2,3}\{4\}$  ratios show enhancement and suppression controlled by

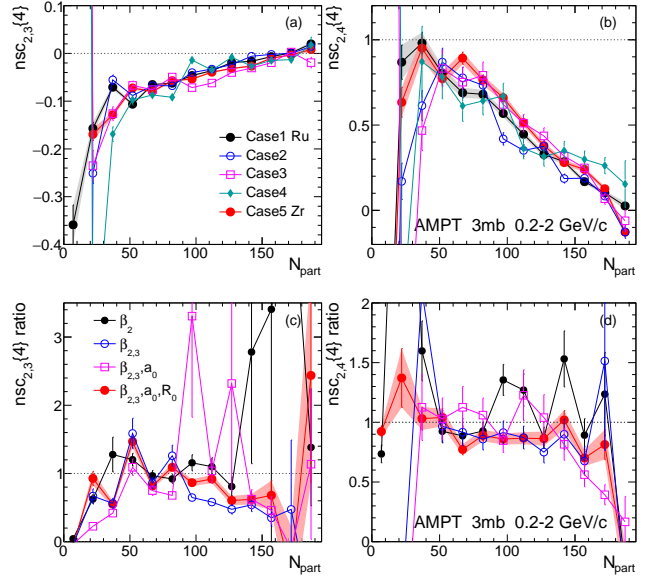


**Fig. 4** Normalized symmetric cumulant  $nsc_{n,m}\{4\}$  (a,b) and the ratios between Ru+Ru and Zr+Zr (c,d) representing the influence of nuclear structures as a function of  $N_{part}$  in  $0.2 < p_T < 2$  GeV/c. The effects of various Woods-Saxon parameters in Table. 1 are shown.

$\beta_2$  and  $\beta_3$  in central collisions, respectively. A cancellation effect between skin thickness and nuclear radius is observed, as we noticed earlier. The overall trends presented here show suppression in central collisions. The  $nsc_{2,4}\{4\}$  shows much clearer effects of nuclear structure parameters. The quadrupole deformation  $\beta_2$  enhances the central collisions and the octupole deformation  $\beta_3$  suppresses the ratios in peripheral collisions. A clear reduction behavior of the neutron skin thickness contribution is observed. After taking into account the influences of all four WS parameters, we briefly summarize the origin of the nuclear structure effect from the AMPT results as follows: 1) The effects of nuclear deformation are mostly concentrated in central collisions, with  $\beta_{2,\text{Ru}}$  and  $\beta_{3,\text{Zr}}$  working in the opposite directions. 2) The diffuseness parameter  $a_0$  and the half-density radius  $R_0$  play a sizeable reduction role in collisions. In general, the predictions of such overall centrality dependence of  $sc_{n,m}\{4\}$  ratios in Fig. 3 are the same as the preliminary results from the STAR experiment [72] and  $nsc_{n,m}\{4\}$  in Fig. 4 can also be studied at the precise level in experiment.

Following by the previous work [47], we extended the shear viscosity effect to the correlated fluctuations of flow harmonics. The effect of the partonic cross section on the ratios of asymmetric cumulant  $asc_{nm,n+m}\{3\}$  between  $^{96}\text{Ru}+^{96}\text{Ru}$  and  $^{96}\text{Zr}+^{96}\text{Zr}$  collisions is shown in Fig. 5. The deviation of these ratios from unity is related to the difference of collective nuclear structure be-

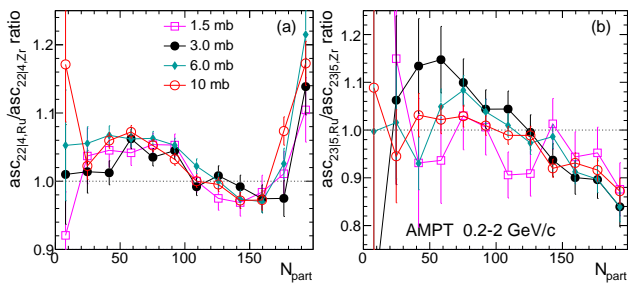


**Fig. 5** Ratios of the asymmetric cumulant  $as_{cnm, n+m}\{3\}$  between  $^{96}\text{Ru}+^{96}\text{Ru}$  and  $^{96}\text{Zr}+^{96}\text{Zr}$ , in particular, different values of the partonic cross sections as a function of  $N_{\text{part}}$  in  $0.2 < p_T < 2 \text{ GeV}/c$ .

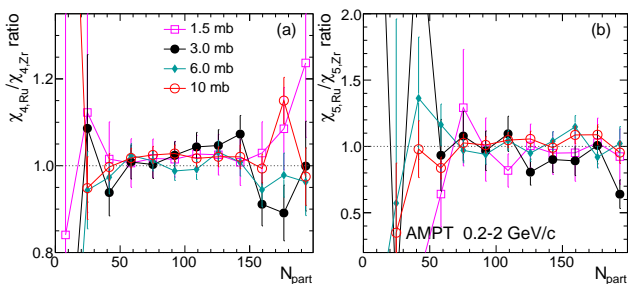


**Fig. 6** Ratios of the nonlinear response coefficients  $\chi_n$  between  $^{96}\text{Ru}+^{96}\text{Ru}$  and  $^{96}\text{Zr}+^{96}\text{Zr}$  in particular different values of the partonic cross sections as a function of  $N_{\text{part}}$  in  $0.2 < p_T < 2 \text{ GeV}/c$ .

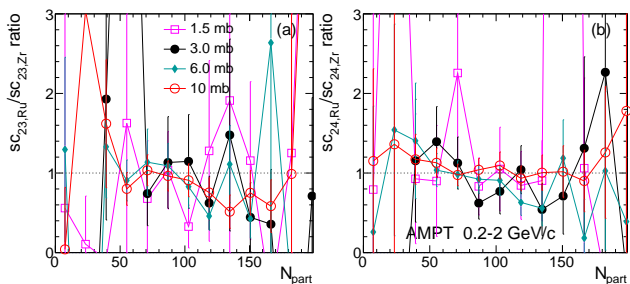


**Fig. 7** Ratios of symmetric cumulant  $sc_{nm}\{4\}$  between  $^{96}\text{Ru}+^{96}\text{Ru}$  and  $^{96}\text{Zr}+^{96}\text{Zr}$  in particular different values of partonic cross-sections as a function of  $N_{\text{part}}$  in  $0.2 < p_T < 2 \text{ GeV}/c$ .

tween Ru and Zr nuclei in terms of quadrupole deformation  $\beta_2$ , octupole deformation  $\beta_3$ , neutron skin  $a_0$ , and nuclear radius  $R_0$ , which has been extensively discussed in detail in Ref. [26]. The ratios show the nonmonotonic behavior and are almost unchanged, implying that the isobar ratios of the multiparticle correlations are insensitive to the medium properties in the final state. On the other hand, the nonlinear coupling coefficients  $\chi_n$  shown in the Fig. 6 also present the similar comparisons. We emphasize that this analysis can be performed directly if our prediction is confirmed by the experiment and other hydrodynamical model calculations. Figure 7

and Fig. 8 show the shear viscosity effect on the ratio of the symmetric cumulant  $sc_{n,m}\{4\}$  and normalized symmetric cumulant  $nsc_{n,m}\{4\}$  and these results imply a negligible shear viscosity effect with large statistical errors.

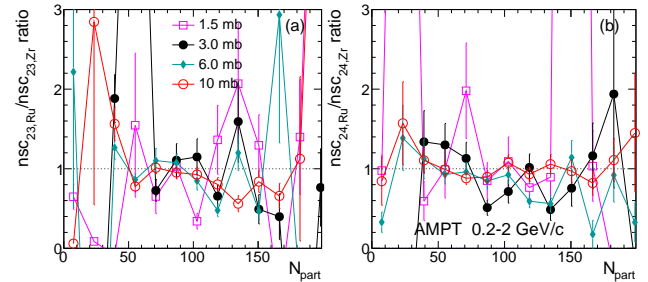


**Fig. 8** Ratios of the normalized symmetric cumulant  $nsc_{nm}\{4\}$  between  $^{96}\text{Ru}+^{96}\text{Ru}$  and  $^{96}\text{Zr}+^{96}\text{Zr}$ , in particular different values of partonic cross sections as a function of  $N_{\text{part}}$  in  $0.2 < p_T < 2 \text{ GeV}/c$ .

## 4 Conclusions

In summary, we studied how the nuclear structure parameters influence the long-range multiparticle correlations and their ratios between  $^{96}\text{Ru}+^{96}\text{Ru}$  and  $^{96}\text{Zr}+^{96}\text{Zr}$  collisions at  $\sqrt{s_{\text{NN}}} = 200 \text{ GeV}$  using AMPT model. We predicted the trends for the aforementioned asymmetric cumulant, the non-linear mode coefficients, and the (normalized-) symmetric cumulants. We observed significant deviations of these ratios from the unity, which were attributed to the difference between the collective nuclear structures of  $^{96}\text{Ru}$  and  $^{96}\text{Zr}$  nuclei. Quadrupole deformation  $\beta_2$  and octupole deformation  $\beta_3$  are found to present the largest influence, and nuclear radius  $R_0$  roughly cancels out the effect of neutron skin  $a_0$ . Moreover, we also showed that the shear viscosity effects on the correlations of different flow harmonics are negligible. These studies provide a complementary tool to quantify the nature of the initial state fluctuations. It could also help us to constrain the nuclear parameters with multiple observables simultaneously. Nevertheless, applying such a possibility to other isobars in the nuclear chart or isobar-like  $^{16}\text{O}+^{16}\text{O}$  and  $^{20}\text{Ne}+^{20}\text{Ne}$  collisions, will effectively permit us to further pursue the many-body properties of nuclear clusters with the advent of modern ab-initio methods in future [73, 74, 75, 76, 77, 78, 79].

## 5 Acknowledgements

The authors thank Somadutta Bhatta and Lumeng Liu for the valuable comments. Z. Wang, J. Chen, Y.-G. Ma and C. Zhang are funded by the National Key Research and Development Program of China under Contract No. 2022YFA1604900, by the National Natural Science Foundation of China under Contracts Nos. 12025501 and 12147101. J. Jia is supported by DOE Research Grant Number DE-SC0024602.

## References

1. Charles Gale, Sangyong Jeon, and Bjoern Schenke. Hydrodynamic Modeling of Heavy-Ion Collisions. *Int. J. Mod. Phys.*, A28:1340011, 2013.
2. Ulrich Heinz and Raimond Snellings. Collective flow and viscosity in relativistic heavy-ion collisions. *Ann. Rev. Nucl. Part. Sci.*, 63:123–151, 2013.
3. Paul Romatschke and Ulrike Romatschke. *Relativistic Fluid Dynamics In and Out of Equilibrium*. Cambridge Monographs on Mathematical Physics. Cambridge University Press, 5 2019.
4. Derek Teaney and Li Yan. Non linearities in the harmonic spectrum of heavy ion collisions with ideal and viscous hydrodynamics. *Phys. Rev. C*, 86:044908, 2012.
5. Scott Pratt, Evan Sangaline, Paul Sorensen, and Hui Wang. Constraining the equation of state of superhadronic matter from heavy-ion collisions. *Phys. Rev. Lett.*, 114:202301, 2015.
6. Sergei A. Voloshin, Arthur M. Poskanzer, and Raimond Snellings. Collective phenomena in non-central nuclear collisions. *Landolt-Bornstein*, 23:293–333, 2010.
7. L. Adamczyk et al. Azimuthal anisotropy in U+U and Au+Au collisions at RHIC. *Phys. Rev. Lett.*, 115(22):222301, 2015.
8. J. Adam et al. Investigation of the linear and mode-coupled flow harmonics in Au+Au collisions at  $\sqrt{s_{NN}} = 200$  GeV. *Phys. Lett. B*, 809:135728, 2020.
9. Mohamed Abdallah et al. Collision-System and Beam-Energy Dependence of Anisotropic Flow Fluctuations. *Phys. Rev. Lett.*, 129(25):252301, 2022.
10. M. I. Abdulhamid et al. Measurements of the Elliptic and Triangular Azimuthal Anisotropies in Central He3+Au, d+Au and p+Au Collisions at sNN=200 GeV. *Phys. Rev. Lett.*, 130(24):242301, 2023.
11. Morad Aaboud et al. Fluctuations of anisotropic flow in Pb+Pb collisions at  $\sqrt{s_{NN}} = 5.02$  TeV with the ATLAS detector. *JHEP*, 01:051, 2020.
12. Jaroslav Adam et al. Correlated event-by-event fluctuations of flow harmonics in Pb-Pb collisions at  $\sqrt{s_{NN}} = 2.76$  TeV. *Phys. Rev. Lett.*, 117:182301, 2016.
13. Albert M Sirunyan et al. Non-Gaussian elliptic-flow fluctuations in PbPb collisions at  $\sqrt{s_{NN}} = 5.02$  TeV. *Phys. Lett. B*, 789:643–665, 2019.
14. Xin-Li Zhao and Guo-Liang Ma. Search for the chiral magnetic effect in collisions between two isobars with deformed and neutron-rich nuclear structures. *Phys. Rev. C*, 106(3):034909, 2022.
15. Dmitri E. Kharzeev, Jinfeng Liao, and Shuzhe Shi. Implications of the isobar-run results for the chiral magnetic effect in heavy-ion collisions. *Phys. Rev. C*, 106(5):L051903, 2022.
16. Fei Li, Yu-Gang Ma, Song Zhang, Guo-Liang Ma, and Qiye Shou. Impact of nuclear structure on the background in the chiral magnetic effect in  $^{96}\text{Ru} + ^{96}\text{Ru}$  and  $^{96}\text{Zr} + ^{96}\text{Zr}$  collisions at  $\sqrt{s_{NN}} = 7.7 - 200$  GeV from a multiphase transport model. *Phys. Rev. C*, 106:014906, 2022.
17. Q. Y. Shou, Y. G. Ma, P. Sorensen, A. H. Tang, F. Videbæk, and H. Wang. Parameterization of Deformed Nuclei for Glauber Modeling in Relativistic Heavy Ion Collisions. *Phys. Lett. B*, 749:215–220, 2015.
18. Giuliano Giacalone, Jiangyong Jia, and Chunjian Zhang. Impact of nuclear deformation on relativistic heavy-ion collisions: Assessing consistency in nuclear physics across energy scales. *Phys. Rev. Lett.*, 127:242301, 2021.
19. Maowu Nie, Chunjian Zhang, Zhenyu Chen, Li Yi, and Jiangyong Jia. Impact of nuclear structure on longitudinal flow decorrelations in high-energy isobar collisions. *Phys. Lett. B*, 845:138177, 2023.
20. Jiangyong Jia. Shape of atomic nuclei in heavy ion collisions. *Phys. Rev. C*, 105(1):014905, 2022.
21. Hao-jie Xu, Wenbin Zhao, Hanlin Li, Ying Zhou, Lie-Wen Chen, and Fuqiang Wang. Probing nuclear structure with mean transverse momentum in relativistic isobar collisions. *Phys. Rev. C*, 108(1):L011902, 2023.
22. Jiangyong Jia. Probing triaxial deformation of atomic nuclei in high-energy heavy ion collisions. *Phys. Rev. C*, 105(4):044905, 2022.
23. Lu-Meng Liu, Chun-Jian Zhang, Jia Zhou, Jun Xu, Jiangyong Jia, and Guang-Xiong Peng. Probing neutron-skin thickness with free spectator neutrons in ultracentral high-energy isobaric collisions. *Phys. Lett. B*, 834:137441, 2022.
24. Lu-Meng Liu, Chun-Jian Zhang, Jun Xu, Jiangyong Jia, and Guang-Xiong Peng. Free spectator nucleons in ultracentral relativistic heavy-ion collisions as a probe of neutron skin. *Phys. Rev. C*, 106:034913, 2022.
25. Shujun Zhao, Hao-jie Xu, Yu-Xin Liu, and Huichao Song. Probing the nuclear deformation with three-particle asymmetric cumulant in RHIC isobar runs. *Phys. Lett. B*, 839:137838, 2023.
26. Jiangyong Jia, Giuliano Giacalone, and Chunjian Zhang. Precision Tests of the Nonlinear Mode Coupling of Anisotropic Flow via High-Energy Collisions of Isobars. *Chin. Phys. Lett.*, 40(4):042501, 2023.
27. Giuliano Giacalone. Observing the deformation of nuclei with relativistic nuclear collisions. *Phys. Rev. Lett.*, 124(20):202301, 2020.
28. Jiangyong Jia, Shengli Huang, and Chunjian Zhang. Probing nuclear quadrupole deformation from correlation of elliptic flow and transverse momentum in heavy ion collisions. *Phys. Rev. C*, 105(1):014906, 2022.
29. Benjamin Bally, Michael Bender, Giuliano Giacalone, and Vittorio Somà. Evidence of the triaxial structure of  $^{129}\text{Xe}$  at the Large Hadron Collider. *Phys. Rev. Lett.*, 128(8):082301, 2022.
30. Govert Nijs and Wilke van der Schee. Inferring nuclear structure from heavy isobar collisions using Trajectum. *SciPost Phys.*, 15(2):041, 2023.
31. Jiangyong Jia and Chunjian Zhang. Scaling approach to nuclear structure in high-energy heavy-ion collisions. *Phys. Rev. C*, 107(2):L021901, 2023.
32. Jinhui Chen et al. Properties of the QCD Matter – An Experimental Review of Selected Results from RHIC BES Program. 7 2024.
33. Hao-jie Xu, Jie Zhao, and Fuqiang Wang. Hexadecapole Deformation of U238 from Relativistic Heavy-Ion Collisions Using a Nonlinear Response Coefficient. *Phys. Rev. Lett.*, 132(26):262301, 2024.



34. Shujun Zhao, Hao-jie Xu, You Zhou, Yu-Xin Liu, and Huichao Song. Exploring the Nuclear Shape Phase Transition in Ultra-Relativistic  $^{129}\text{Xe}+^{129}\text{Xe}$  Collisions at the LHC. 3 2024.
35. Hao-jie Xu, Hanlin Li, Ying Zhou, Xiaobao Wang, Jie Zhao, Lie-Wen Chen, and Fuqiang Wang. Measuring neutron skin by grazing isobaric collisions. *Phys. Rev. C*, 105(1):L011901, 2022.
36. Jiaxing Zhao and Shuzhe Shi. Detecting nuclear mass distribution in isobar collisions via charmonium. *Eur. Phys. J. C*, 83(6):511, 2023.
37. Nicolas Fortier, Sangyong Jeon, and Charles Gale. Comparisons and Predictions for Collisions of deformed  $^{238}\text{U}$  nuclei at  $\sqrt{s_{NN}} = 193$  GeV. 8 2023.
38. Nicolas Fortier, Sangyong Jeon, and Charles Gale. Heavy-Ion Collisions as Probes of Nuclear Structure. 5 2024.
39. Chunjian Zhang, Shengli Huang, and Jiangyong Jia. Longitudinal Structure of Quark-Gluon Plasma Unveiled Through Nuclear Deformations. 5 2024.
40. Jiangyong Jia, Shengli Huang, Chunjian Zhang, and Somadutta Bhatta. Sources of longitudinal flow decorrelations in high-energy nuclear collisions. 8 2024.
41. Niseem Magdy. Impact of nuclear deformation on collective flow observables in relativistic U+U collisions. *Eur. Phys. J. A*, 59(3):64, 2023.
42. Imaging Shapes of Atomic Nuclei in High-Energy Nuclear Collisions. 1 2024.
43. Chunjian Zhang. An overview of new measurements of flow, chirality, and vorticity from STAR experiment. In *10th International Conference on New Frontiers in Physics*, 3 2022.
44. Georges Aad et al. Correlations between flow and transverse momentum in Xe+Xe and Pb+Pb collisions at the LHC with the ATLAS detector: A probe of the heavy-ion initial state and nuclear deformation. *Phys. Rev. C*, 107(5):054910, 2023.
45. Shreyasi Acharya et al. Characterizing the initial conditions of heavy-ion collisions at the LHC with mean transverse momentum and anisotropic flow correlations. *Phys. Lett. B*, 834:137393, 2022.
46. Shreyasi Acharya et al. Exploring nuclear structure with multiparticle azimuthal correlations at the LHC. 9 2024.
47. Chunjian Zhang, Somadutta Bhatta, and Jiangyong Jia. Ratios of collective flow observables in high-energy isobar collisions are insensitive to final-state interactions. *Phys. Rev. C*, 106(3):L031901, 2022.
48. Benjamin Bally et al. Imaging the initial condition of heavy-ion collisions and nuclear structure across the nuclide chart. 9 2022.
49. Haojie Xu. Constraints on Neutron Skin Thickness and Nuclear Deformations Using Relativistic Heavy-ion Collisions from STAR. *Acta Phys. Polon. Supp.*, 16(1):1–A30, 2023.
50. Chunjian Zhang. Imaging the structure of atomic nuclei in high-energy nuclear collisions from STAR experiment. 9 2024.
51. Zi-Wei Lin, Che Ming Ko, Bao-An Li, Bin Zhang, and Subrata Pal. A Multi-phase transport model for relativistic heavy ion collisions. *Phys. Rev. C*, 72:064901, 2005.
52. Xin-Nian Wang and Miklos Gyulassy. hijing: A monte carlo model for multiple jet production in pp, pA, and AA collisions. *Phys. Rev. D*, 44:3501–3516, 1991.
53. Bin Zhang. ZPC 1.0.1: A Parton cascade for ultrarelativistic heavy ion collisions. *Comput. Phys. Commun.*, 109:193–206, 1998.
54. Yuncun He and Zi-Wei Lin. Improved Quark Coalescence for a Multi-Phase Transport Model. *Phys. Rev. C*, 96(1):014910, 2017.
55. Tianhao Shao, Jinhui Chen, Che Ming Ko, and Zi-Wei Lin. Enhanced production of strange baryons in high-energy nuclear collisions from a multiphase transport model. *Phys. Rev. C*, 102(1):014906, 2020.
56. Bao-An Li and Che Ming Ko. Formation of superdense hadronic matter in high-energy heavy ion collisions. *Phys. Rev. C*, 52:2037–2063, 1995.
57. P. Möller, A. J. Sierk, T. Ichikawa, and H. Sagawa. Nuclear ground-state masses and deformations: FRDM(2012). *Atom. Data Nucl. Data Tabl.*, 109-110:1–204, 2016.
58. Chunjian Zhang and Jiangyong Jia. Evidence of Quadrupole and Octupole Deformations in Zr96+Zr96 and Ru96+Ru96 Collisions at Ultrarelativistic Energies. *Phys. Rev. Lett.*, 128(2):022301, 2022.
59. Jiangyong Jia, Giuliano Giacalone, and Chunjian Zhang. Separating the Impact of Nuclear Skin and Nuclear Deformation in High-Energy Isobar Collisions. *Phys. Rev. Lett.*, 131(2):022301, 2023.
60. Zi-wei Lin and C. M. Ko. Partonic effects on the elliptic flow at RHIC. *Phys. Rev. C*, 65:034904, 2002.
61. Zi-Wei Lin and Liang Zheng. Further developments of a multi-phase transport model for relativistic nuclear collisions. *Nucl. Sci. Tech.*, 32(10):113, 2021.
62. Hai Wang and Jin-Hui Chen. Anisotropy flows in Pb–Pb collisions at LHC energies from parton scatterings with heavy quark trigger. *Nucl. Sci. Tech.*, 33(2):15, 2022.
63. Chao Zhang, Liang Zheng, Shusu Shi, and Zi-Wei Lin. Resolving the RpA and v2 puzzle of D0 mesons in p–Pb collisions at the LHC. *Phys. Lett. B*, 846:138219, 2023.
64. Zaining Wang, Jinhui Chen, Hao-jie Xu, and Jie Zhao. Systematic investigation of the nuclear multipole deformations in U+U collisions with a multi-phase transport model. *Phys. Rev. C*, 110(3):034907, 2024.
65. Jun Xu and Che Ming Ko. Pb-Pb collisions at  $\sqrt{s_{NN}} = 2.76$  TeV in a multiphase transport model. *Phys. Rev. C*, 83:034904, 2011.
66. Ante Bilandzic, Raimond Snellings, and Sergei Voloshin. Flow analysis with cumulants: Direct calculations. *Phys. Rev. C*, 83:044913, 2011.
67. Jiangyong Jia, Mingliang Zhou, and Adam Trzupek. Revealing long-range multiparticle collectivity in small collision systems via subevent cumulants. *Phys. Rev. C*, 96(3):034906, 2017.
68. Zhiyong Lu, Mingrui Zhao, Xiaomei Li, Jiangyong Jia, and You Zhou. Probe nuclear structure using the anisotropic flow at the Large Hadron Collider. *Eur. Phys. J. A*, 59(11):279, 2023.
69. Niseem Magdy. Characterizing initial- and final-state effects of relativistic nuclear collisions. *Phys. Rev. C*, 107(2):024905, 2023.
70. Jia-Lin Pei, Guo-Liang Ma, and Adam Bzdak. Symmetric cumulant sc2,44 and asymmetric cumulant ac23 from transverse momentum conservation and flow. *Phys. Rev. C*, 110(2):024901, 2024.
71. Shreyasi Acharya et al. Linear and non-linear flow modes in Pb-Pb collisions at  $\sqrt{s_{NN}} = 2.76$  TeV. *Phys. Lett. B*, 773:68–80, 2017.
72. Chunjian Zhang, for the STAR Collaboration, WPCF 2022, Measurement of nuclear deformation in relativistic heavy-ion collisions at STAR.
73. Giuliano Giacalone et al. The unexpected uses of a bowling pin: exploiting  $^{20}\text{Ne}$  isotopes for precision characterizations of collectivity in small systems. 2 2024.

74. Giuliano Giacalone et al. The unexpected uses of a bowling pin: anisotropic flow in fixed-target  $^{208}\text{Pb}+^{20}\text{Ne}$  collisions as a probe of quark-gluon plasma. 5 2024.
75. Chunjian Zhang, Jinhui Chen, Giuliano Giacalone, Shengli Huang, Jiangyong Jia, and Yu-Gang Ma. *Ab-initio* nucleon-nucleon correlations and their impact on high energy  $^{16}\text{O}+^{16}\text{O}$  collisions. 4 2024.
76. Xin-Li Zhao, Guo-Liang Ma, You Zhou, Zi-Wei Lin, and Chao Zhang. Nuclear cluster structure effect in  $^{16}\text{O}+^{16}\text{O}$  collisions at the top RHIC energy. 4 2024.
77. Yuanyuan Wang, Shujun Zhao, Boxing Cao, Hao-jie Xu, and Huichao Song. Exploring the compactness of  $\alpha$  clusters in O16 nuclei with relativistic O16+O16 collisions. *Phys. Rev. C*, 109(5):L051904, 2024.
78. Hai-Cheng Wang, Song-Jie Li, Lu-Meng Liu, Jun Xu, and Zhong-Zhou Ren. Deformation probes for light nuclei in their collisions at relativistic energies. *Phys. Rev. C*, 110(3):034909, 2024.
79. Lu-Meng Liu, Song-Jie Li, Zhen Wang, Jun Xu, Zhong-Zhou Ren, and Xu-Guang Huang. Probing configuration of  $\alpha$  clusters with spectator particles in relativistic heavy-ion collisions. *Phys. Lett. B*, 854:138724, 2024.